Electromigration Study of Plasma Etched Copper Lines with Copper Oxide Capping Layers

To cite this article: Jia Quan Su and Yue Kuo 2020 *ECS Trans.* **97** 51

View the article online for updates and enhancements.

PRIME
PACIFIC RIM MEETING
ON ELECTROCHEMICAL
AND SOLID STATE SCIENCE
2020

Abstract Submission
DEADLINE EXTENDED:
May 29, 2020

Honolulu, HI | October 4-9, 2020

Electromigration Study of Plasma Etched Copper Lines with Copper Oxide Capping Layers

Jia Quan Su, Yue Kuo[*]

Thin Film Nano & Microelectronics Research Laboratory, Texas A&M University, College Station, Texas 77843, U.S.A. *yuekuo@tamu.edu

The electromigration failure phenomena of the plasma etched copper line with a copper oxide capping layer has been studied. The copper oxide prepared by the oxygen plasma oxidation method covers the entire copper stack. The failure of this kind of structure was determined from the resistance change with the stress time. The line temperature was calculated accordingly assuming the adiabatic condition, i.e., the dissipation of Joule heat to the glass substrate and environment was negligible. The surface color of the line changes with the stress time. The composition and color of the copper oxide passivation layer were characterized and correlated to the Joule heating. The color change can be an effective reference to predict the line failure location and time. In summary, the copper oxide passivation layer can be easily formed into the self-aligned structure and the line failure process can be detected from the color change.

Introduction

Copper (Cu) is a widely used interconnect material in very high density integrated circuits (ICs) and large-area thin film transistor (TFT) arrays due to advantages of high conductivity, negligible hillocks formation and high resistance to electromigration (EM) (1-3). Conventionally, chemical-mechanical polishing (CMP) is the most popular method for the fabrication of Cu interconnect lines in ICs (3,4). However, CMP is a complicated process that involves environmentally unfriendly chemicals, e.g., strong oxidants, surfactants, and nanoparticles. The end point is difficult to detect. The dishing phenomenon is commonly observed in the CMP fabricated Cu lines (5-7). Moreover, CMP cannot be applied to the fabrication of the large-area TFT array because the surface of the glass substrate is not as flat as that of the silicon wafer.

Plasma etching has been widely used in preparing small geometry metal interconnect lines since it provides well controlled profiles with the tight critical dimension (CD) control (8-12). However, the conventional plasma etching method is not applicable to Cu because of the low Cu halide vapor pressure (13). Kuo's group first reported a novel plasma-based Cu etch process. It consists of two steps: a high rate plasma Cu chlorination or bromination reaction that converts the metallic Cu film into a porous compound layer and a sequential HCl solution dipping step that dissolves the Cu compound instantaneously (14-16). The plasma reaction can be carried at room temperature in a parallel-plate reactor. This method has been used in preparing the BiCMOS chip as well as the 15" thin film transistor liquid crystal display (TFT LCD) (17-19). Cu was etched into sub 0.3 µ patterns using this method (20).

The reliability of a metal line is usually investigated with the electromigration (EM) method. A high density current is applied to the line until it is broken from the formation and connection of voids (21). The first study of the EM failure of the plasma-etched Cu line was reported by Liu and Kuo (22). Recently, the influence of Cu line geometry, e.g., width and length, on the EM lifetime was reported (23).

A barrier layer is often required to provide good adhesion between the Cu film and the substrate. Titanium-tungsten (TiW) and molybdenum (Mo) are good barrier materials for the glass substrate and easily etched with plasma processes (23-29).

There are studies on the capping layer effect on the EM failure of the damascene Cu line (30,31). The CMP prepared Cu line is embedded in the dielectric trench structure. On the other hand, the plasma etched Cu line is free standing similar to the plasma etched aluminum or other metal lines. There are studies showing that interface structure can be critical to the EM failure life of the metal line. For example, the TiW and Mo capping layers can reduce the lifetime of the plasma etched Cu line (32-35). The high line temperature during the high current stress caused the diffusion of Cu to the capping layer, which enhanced the void formation in the bulk film and therefore, the breakage of the line.

In this work, we investigated the effect of the copper oxide (CuO_x) capping layer on the failure mechanism of the Cu line. The CuO_x film, which may exist in CuO, Cu_2O, and other forms, has several advantages over other types of capping material. Although the CuO_x film can be easily formed using various methods (36-42), it can be simply formed by the plasma oxidation of the Cu line at room temperature. All the exposed regions, e.g., the top and sidewalls, are converted into CuO_x. It is more economic to form CuO_x by oxidation than by depositing a separate layer that needs additional patterning and etching steps. Furthermore, as shown in Table 1, it is hard to diffuse Cu through the CuO_x layer because it requires a relative large activation energy, e.g., larger than those through the grain boundary and the interface (21,43,44).

Table 1. Activation energies (E_A) of different diffusion paths in Cu samples.

Diffusion path	E_A (eV)
Surface	0.8 ~ 0.9
Grain boundaries	0.88 ~ 0.95
Thermal oxides	1.2
Dislocations	1.2 ~ 1.5
Bulk Cu	2.2

Experimental

Sample preparation

The Mo/Cu stack was prepared first. A 25 nm thick Mo barrier film was sputter deposited at 100 W, 5 mTorr in Ar for 30 minutes on the dilute HF cleaned Corning glass. The Cu film was then sputter deposited on top of the Mo layer at 80W and 10 mTorr in Ar. The sample was lithographically defined into a 4-probe pattern using a mask aligner (Quintel Corporation Q-4000 Series). Before the Cu etch, the sample was dipped in a diluted HCl solution ($HCl:H_2O$=1:4 v/v) to remove the native oxide (32). The Cu layer was completely converted into the $CuCl_x$ film by exposing to the CF_4/HCl 5/20 sccm

plasma at 70 mTorr, and 600 W for 2 minutes in a PlasmaTherm 700C system operated in reactive ion etching (RIE) mode. Then, the sample was dipped in a diluted HCl solution (HCl:H$_2$O=1:8 v/v) for 1 minute to dissolve the CuCl$_x$ film. Subsequently, the Mo barrier layer was etched under the condition of CF$_4$/O$_2$ 10/10 sccm at 60 mTorr, 600 W for 2 minutes. After the photoresist layer was stripped off with the AZ400T stripper, the sample was exposed to the O$_2$ plasma at 100 W and 200 mTorr for 3 minutes in the PlasmaTherm 700C system operated in plasma etching (PE) mode. The exposed Cu was oxidized to CuO$_x$. Samples without the CuO$_x$ capping layer were also prepared for comparison.

EM stress tests and sample analyses

For the line reliability study, the 2 μm to 60 μm wide samples were loaded on a probe station (Signatone S-1160) and stressed at a constant current density (J) between 2.57×10^5 and 1.54×10^6 Amp/cm^2. The current was provided by an Agilent E3645A DC power supply and controlled with a customized Labview program. The resistance vs. stress time (t) curve was recorded. The color and physical appearance of the Cu line were monitored through an optical microscope. The surface composition and structure of the sample were analyzed using the x-ray photoelectron spectroscopy (XPS).

Line temperature estimation

The temperature of the Cu line changes with the EM stress time due to the Joule heating effect. It could be estimated following the JEDEC standard guidelines of JESD33-B by taking into consideration of the system configuration (45). In the calculation, it is assumed that the initial line temperature and resistance are constant. However, since the substrate in our study was the low thermal conductivity glass, the above assumption was modified. For example, the Joule heat generated in one stage was included in the calculation of the temperature at the next stage. An iteration method was applied to calculate the line temperature at stage i, i.e., T_i, by taking into account of all parameters at the previous stage, i.e., i-1. The modified equation used for the temperature calculation is shown below:

$$T_i = \frac{R(T_i) - R(T_{i-1})}{R(T_{ref}) \times TCR(T_{ref})} + T_{i-1} \qquad [1]$$

where $R(T_i)$ is the resistance at temperature T_i, $R(T_{i-1})$ is the resistance at temperature T_{i-1}, $R(T_{ref})$ is the resistance at the reference temperature, i.e., 20°C, $TCR(T_{ref})$ is the temperature coefficient of resistance at the reference temperature. The $TCR(T_{ref})$ value was calibrated by the following equation.

$$TCR(T_{ref}) = \frac{1}{R(T_{ref})} \times \frac{\Delta R}{\Delta T} \qquad [2]$$

where ΔR is the resistance difference and ΔT is the temperature difference before and after the temperature change. The chuck temperature was controlled through a heat exchanger (Signatone Model S-1060R) and the resistance of the Cu line was recorded constantly by a customized Labview program.

In equation 1, the temperature ramps up linearly with the line resistance. The deviation of temperature from linearity becomes non-negligible when the temperature exceeds

230°C (45). Therefore, in the high temperature region, the calibrated temperature (T_{cal}) was obtained by applying a correction factor $F_{corr}(T_i)$ using the following equations:

$$T_{cal} = F_{corr}(T_i) \times T_i \qquad [3]$$

$$F_{corr}(T_i) = 1.0167 - 8.39751 \times 10^{-5}T_i - 3.74768 \times 10^{-8}T_i^2 \quad [4]$$

Results and Discussions

CuO$_x$ capped sample structure and physical appearance

Figure 1 shows a cross-sectional view of the Cu stack used in this study. The top and sidewalls of the Cu line were enclosed with the CuO$_x$ passivation layer.
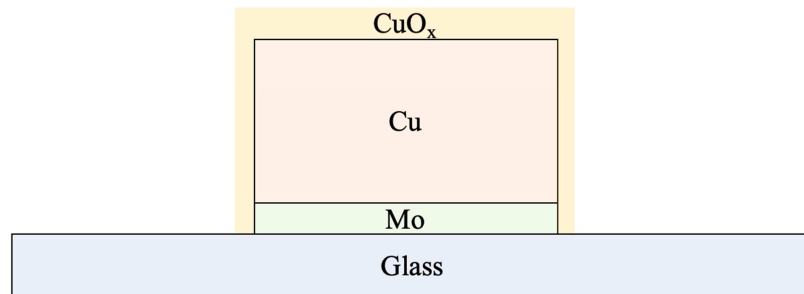

Figure 1. Cu stack used in lifetime study.

Figure 2 shows a top view of the Mo/Cu/CuO$_x$ line (a) before and (b) after the CuO$_x$ passivation was formed. The original beige colored Cu was changed to light green. The color change is due to the transmission and reflection of light through the added CuO$_x$ layer.
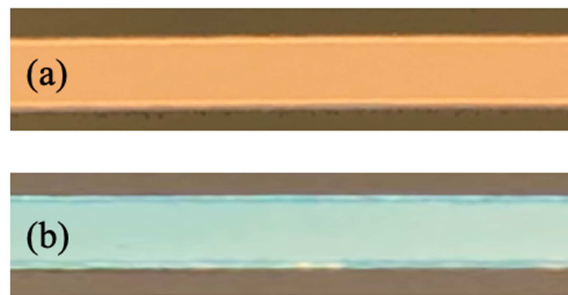

Figure 2. Colors of Cu lines (a) before and (b) after addition of CuO$_x$ layer.

Image of broken spot in CuO$_x$ capped Cu line

Figure 3 shows a scanning electron microscope (SEM) image of the broken section of a Mo/Cu/CuO$_x$ line after the EM stress. Multiple bumps are observed, which is generated from the difference in the secondary electron signals (46,47). The darker color is the groove-like depression region where the secondary electron signals are blocked. The

distribution of extruding region and voiding region is consistent with the stress evolution model proposed by Korhonen *et al.* (48,49). At the region closer to the cathode, the local stress is tensile which causes a net depletion of atoms. When the stress value exceeds a critical limit, voids are formed and connected to cause the discontinuity of the line. On the contrary, the anode region has the compressive stress, which causes the net accumulation of atoms leading to the formation of an extruded surface topography.
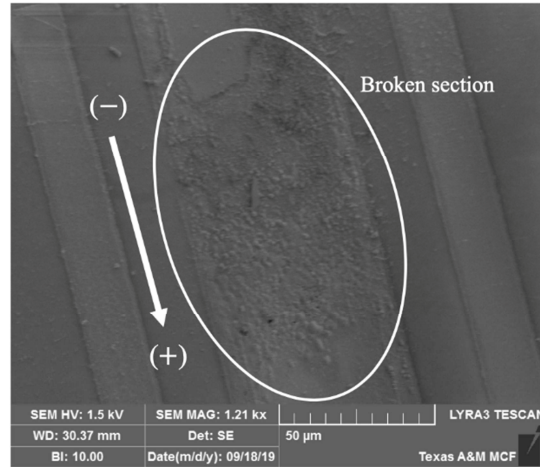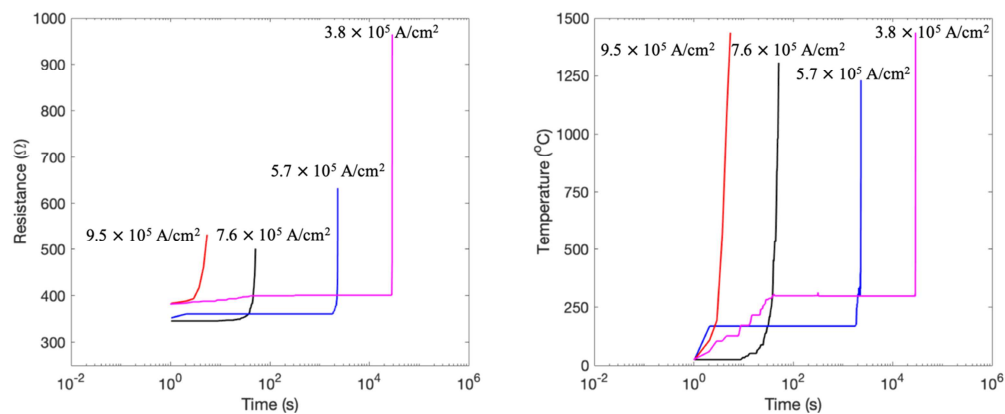

Figure 3. SEM image of a broken section of Mo/Cu/CuO$_x$ line stressed at $J = 1.03 \times 10^6$ A/cm^2.

Changes of resistance and temperature with EM stress time

The resistance vs. time (*R-t*) and temperature vs. time (*T-t*) curves of the Cu line can be used to interpret the physical process of the EM failure phenomena. Figure 4(a) shows *R-t* curves of Mo/Cu/CuO$_x$ lines stressed under various current densities, i.e., $J = 3.8 \times 10^5$, 5.7×10^5, 7.6×10^5, and 9.5×10^5 A/cm^2, separately. In the early stage, the line resistance gradually increases with the stress time. Near the line broken time, the resistance increases drastically. The trend of *R-t* curve change is consistent with previous report on other Cu-based interconnection lines (22,31-34). In previous studies, the line breakage was initiated from the void formation at the current flux divergence area (21,28,50,51). Fig. 4(a) shows that the line stressed at large current densities has a shorter breakage time than that stressed at small current densities. This can be explained by the enhanced void formation at the large current stress current, which causes the quick breakage of the line.
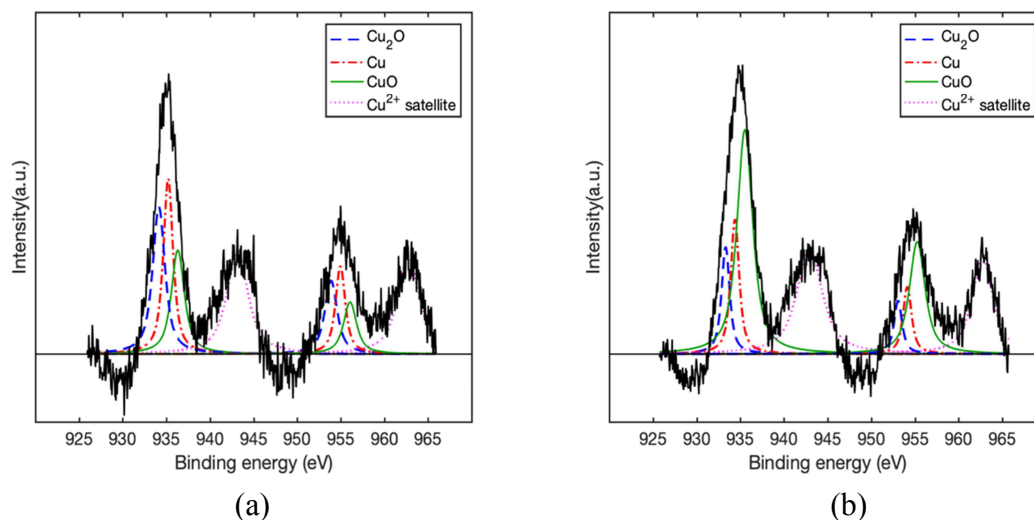
(a) (b)

Figure 4. (a) *R-t* and (b) *T-t* curves of Mo/Cu/CuO$_x$ (25 nm/135 nm/40 nm) lines stressed at $J = 3.8 \times 10^5$, 5.7×10^5, 7.6×10^5, and 9.5×10^5 A/cm^2. $W = 14$ μm, and $L = 800$ μm.

Figure 4(b) shows the *T-t* curves calculated from *R-t* curves in Fig. 4(a). The temperature increased at a low rate at the beginning and increased drastically near the breakage point. The larger the current density is, the faster the temperature increasing rate is. The amount of heat accumulated increased with time because of the poor thermal conductivity of the glass substrate. For example, the temperature of the line stressed at $J = 5.7 \times 10^5$ A/cm^2 exceeded 1000ºC at the breakage point. The high temperature could enhance the mass flux of Cu diffusion at the grain junctions, which accelerates the void formation and the line breakage process (50).

Change of chemical structure of CuO$_x$ capping layer after EM stress

Figure 5 shows the XPS Cu 2p spectra of samples (a) before and (b) after the EM stress. The Cu peaks were deconvoluted to Cu, Cu$_2$O, and CuO sub peaks similar to those in refs. 52, 53, and 54. The Cu 2p$_{1/2}$ binding energies (BE's) of metallic Cu, Cu$_2$O, and CuO are 954.13 eV, 953.07 eV, and 955.27 eV, respectively. The Cu 2p$_{3/2}$ BE's of metallic Cu, Cu$_2$O, and CuO are 934.38 eV, 933.32 eV, and 935.51 eV, respectively. The two satellite peaks located near BE 943 eV and 963 eV could be referred to the Cu^{2+} component (52-55).

(a) (b)

Figure 5. XPS Cu 2p peaks of Mo/Cu/CuO$_x$ surfaces (a) before and (b) after EM stress at $J = 2.8 \times 10^5$ A/cm^2 for 12 minutes.

Table 2 lists area ratios of metallic Cu, Cu$_2$O, and CuO to the total Cu amount as well as to the metallic Cu component before and after the EM stress. After the EM stress test, the CuO ratio increased. At the same time, the metallic Cu and the Cu$_2$O ratios decreased. The increase of the CuO ratio could be contributed by the enhanced oxidation of Cu from

Table 2. XPS area ratios of Cu components in the CuO$_x$ capping layer.

Component (area ratio)	Before EM	After EM
Cu$_2$O/total Cu	0.37	0.16
Metallic Cu/total Cu	0.35	0.21

CuO/total Cu	0.28	0.64
Cu$_2$O/metallic Cu	1.06	0.76
CuO/metallic Cu	0.80	3.05
Cu$_2$O/CuO	1.32	0.25

Joule heating. In addition, the metallic Cu ratio decreased by 40%, which is due to the oxidation of the Cu component. Also, the CuO/metallic Cu ratio increased, the Cu$_2$O/metallic Cu ratio decreased, and the Cu$_2$O/CuO ratio decreased after EM testing. It is possible that the Cu$_2$O component was further oxidized into CuO in the process. Therefore, CuO$_x$ is an effective capping layer that not only hinders the diffusion of metallic Cu but also converts it into the oxide form.

Surface color change with EM stress time

Surface color changes of Cu lines with and without the CuO$_x$ capping layer during the current stress were monitored. Figure 6 shows images of a Mo/Cu line and a Mo/Cu/CuO$_x$ line with similar line width and thickness at different stress times. In Figure 6(a), the original uncapped line was of the beige color. The color was darkened with the increase of the stress time. Then, a bright spot appeared at the axial diverge point where the line was later broken and the dark region appeared. The similar phenomenon was observed previously (33,35). The color change of the uncapped line could be caused by the enhanced oxidation of the Cu surface from the rise of the temperature, which was accompanied with the increase of the line resistance (56-59). In addition, the line swelled slightly near the breakage point due to the high local high temperature caused line expansion. In Figure 6(b), the color of the capped Cu line did not change much until near the breakage time when the bright spot appeared and an embedded dark region was observed. The latter quickly expanded to become the line breakage point. The color change of the CuO$_x$ capped Cu line could be due to the composition change. Since the bright region of both capped and uncapped line appeared before the line was broken, this phenomenon could be an effective reference for the prediction of the line failure location and time.
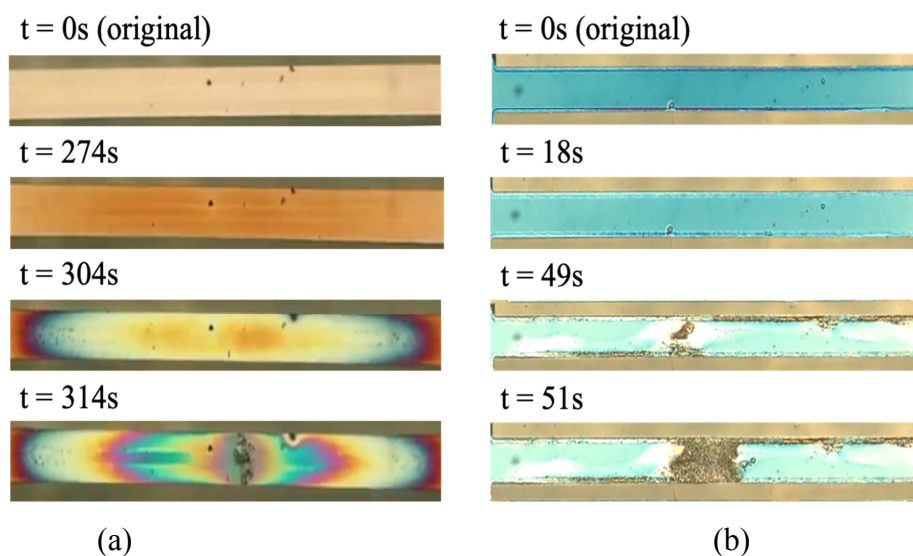

t = 0s (original)

t = 274s

t = 304s

t = 314s

t = 0s (original)

t = 18s

t = 49s

t = 51s

(a)   (b)

Figure 6. Top views of (a) Mo (25 nm)/Cu (125 nm) lines (W = 55 μm, J = 1.1 × 10^6 A/cm^2) and (b) Mo (25 nm)/Cu (135 nm)/CuO$_x$ (40 nm) lines (W = 58 μm, J = 4.1 × 10^5 A/cm^2) at different stress times.

Conclusion

The EM line failure phenomena of the CuO$_x$ capped Cu lines was investigated. The line failure process is consistent with the stress evolution model, i.e., the high tensile stress near the cathode caused the net depletion of atoms. The time-dependent resistance change confirmed the void formation and merging mechanism of the line failure. The line temperature change was calculated from the resistance change assuming the adiabatic condition. Surface analysis of the CuO$_x$ capping layer indicated less metallic Cu in the CuO$_x$ capping layer after the EM stress test. The color of the CuO$_x$ capped Cu lines changed with the EM stress time, which was caused by the surface composition change. The surface color change could be a useful reference for the line failure location and time. In summary, CuO$_x$ can be an effective passivation layer for the Cu line. It serves as a buffer layer to hinder the Cu diffusion to the adjacent layer.

Acknowledgments

References

1. National Technology Roadmap for Semiconductors (NTRS), SIA, (1997).
2. Y. Kuo, *ECS Interface*, **22**(1), 55-61 (2013).
3. J. Proost, T. Hirato, T. Furuhara, K. Maex and J.-P. Celis, *J. Appl. Phys.*, **87**(6), 2792-2802 (2000).
4. C. S. Hau-Riege, S. P. Hau-Riege and A. P. Marathe, *J. Appl. Phys.*, **96**(10), 5792-5796 (2004).
5. C. Yu, P. C. Fazan, V. K. Mathews and T. T. Doan, , *Appl. Phys. Lett.*, **61**(11), 1344-1346 (1992).
6. M. Fayolle and F. Romagna, *Microelectronic Eng.*, **37**, 135-141 (1997).
7. R. Chang, Y. Cao and C. J. Spanos, *IEEE Trans. on Electron Dev.*, **51**(10), 1577-1583 (2004).
8. P. M. Schaible, W. C. Metzger and J. P. Anderson, *J. Vacuum Science and Technology*, **15**(2), 334-337 (1978).
9. D. A. Danner, M. Dalvie and D. W. Hess, *J. Electrochem. Soc.*, **134**(3), 669-673 (1987).
10. Y. Kuo and J.R. Crowe, *J. Vacuum Science and Technology A*, **8**(3), 1529-1532 (1990).
11. P. E. Riley, *J. Electrochem. Soc.*, **140**(5), 1518-1522 (1993).
12. D. J. Cooperberg, V. Vahedi and R. A. Gottscho, *J. Vacuum Science and Technology A*, **20**(5), 1536-1556 (2002).

13. H. Miyazaki, K. Takeda, N. Sakuma, S. Kondo, Y. Homma and K. Hinode., *J. Vacuum Science and Technology B*, **15**(2), 237-240 (1997).
14. Y. Kuo and S. Lee, *Japan J. of Appl. Phys.*, **39**(3A), L188 (2000).
15. S. Lee and Y. Kuo, *J. Electrochem. Soc.*, **148**(9), G524-G529 (2001).
16. Y. Kuo and S. Lee, *Appl. Phys. Lett.*, **78**(7), 1002-1004 (2001).
17. Y. Kuo and S. Lee, *Vacuum* **74(**3-4), 473-477 (2004).
18. Y. Kuo, Proc. 6th Intl. Conf. Reactive Plasmas & 23rd Symp. Plasma Processing, 29-30 (2006).
19. J. Yang, Y. Ahn, J. Bang, W. Ryu, J. Kim, J. Kang, M. S. Yang, I. Kang and I. Cung, *ECS Trans.*, **16**(9), 13 (2008).
20. Y. Kuo, J. Q. Su, M. Li and T. Yuan, XXXIV International Conference on Phenomena in Ionized Gases (XXXIV ICPIG), 10th International Conference on Reactive Plasmas (ICRP-10), Abst. OR19AM-B02, Sapporo, Hokkaido, Japan, July 14-19, (2019).
21. C. S. Hau-Riege, *Microelectronics Reliability*, **44**(2), 195-205 (2004).
22. G. Liu and Y. Kuo, *J. Electrochem. Soc.*, **156**(7), H579-H589 (2009).
23. M. Li and Y. Kuo, *ECS. Trans.*, **86**(8), 41-47 (2018).
24. C. Ryu, H. Lee, K.-W. Kwon, A. LS. Loke and S. S. Wong, *Solid State Technology*, **42**(4), 53-56 (1999).
25. S. Song, Y. Liu, D. Mao, H. Ling and M. Li, *Thin Solid Films*, **476**(1), 142-147 (2005).
26. J.-C. Chuang, S.-L. Tu and M.-C. Chen, *Thin Solid Films*, **346**(1-2), 299-306 (1999).
27. Y. Kuo, *J. Electrochem. Soc.*, **137**(6), 1907-1911 (1990).
28. Y. Kuo and J. R. Crowe, *J. Vacuum Science and Technology A*, **8**(3), 1529-1532 (1990).
29. G. Liu and Y. Kuo, *J. Electrochem. Soc.*, **154**(7), H653-H658 (2007).
30. M. C. Kang, Y. J. Kim and J. J. Kim, *Electrochemical and Solid-State Letters.* **12**(9), H340-H343 (2009).
31. C-K. Hu, L. Gignac, E. Liniger, B. Herbst, D. L. Rath, S. T. Chen, S. Kaldor, A. Simon and W.-T. Tseng, *Appl. Phys. Lett.*, **83**(5), 869-871 (2003).
32. M. Li, J. Q. Su and Y. Kuo, *ECS. Trans.*, **89**(3), 87-92 (2019).
33. J. Q. Su, M. Li and Y. Kuo, *ECS. Trans.*, **90**(1), 65-72 (2019).
34. M. Li, J. Q. Su and Y. Kuo, *ECS. Trans.*, **92**(5), 9-16 (2019).
35. J. Q. Su, M. Li, Y. Kuo and S. Hamaguchi, *ECS. Trans.*, **92**(5), 39-46 (2019).
36. R. V. Kumar, R. Elgamiel, Y. Diamant and A. Gedanken, *Langmuir*, **17**(5), 1406-1410 (2001).
37. W. Wang, Y. Zhan, X. Wang, Y. Liu, C. Zheng and G. Wang, *Mater. Res. Bull.*, **37**(6), 1093-1100 (2002).
38. X. Jiang, T. Herricks and Y. Xia, *Nano Lett.*, **2**(12), 1333-1338 (2002).
39. C.-T. Hsieh, J.-M. Chen, H.-H. Lin and H.-C. Shih, *Appl. Phys. Lett.*, **82**(19), 3316-3318 (2003).
40. W. Wang, Z. Liu, Y. Liu, C. Xu, C. Zheng and G. Wang, *Appl. Phys. A*, **76**(3), 417-420 (2003).
41. W.-T. Yao, S.-H. Yu, Y. Zhou, J. Jiang, Q.-S. Wu, L. Zhang and J. Jiang, *J. Phys. Chem. B*, **109**(29), 14011-14016 (2005).
42. H. Wu, D. Lin and W. Pan, *Appl. Phys. Lett.*, **89**(13), 133125 (2006).
43. G. Raghavan, C. Chiang, P. B. Anders, S.-M. Tzeng, R. Villasol, G. Bai, M. Bohr and D. B. Fraser, *Thin Solid Films*, **262**(1-2), 168-176 (1995).

44. K.-D. Lee, E. T. Ogawa, H. Matsuhashi, P. R. Justison, K.-S. Ko and P. S. Ho, *Appl. Phys. Lett.*, **79**(20), 3236-3238 (2001).
45. EIA/JESD33-B, Standard Method of Measuring and Using the Temperature Coefficient of Resistance to Determine the Temperature of a Metallization Line (2004).
46. J. E. Castle and P. A. Zhdan, *J. Phys. D: Appl. Phys.*, **30**(5), 722-740 (1997).
47. Y. Homma, M. Tomita and T. Hayashi, *Surface Sci.*, **258**(1-3), 147-152 (1991).
48. M. A. Korhonen, P. Borgesen, K. N. Tu and C.-Y. Li, *J. Appl. Phys.,* **73**(8), 3790-3799 (1993).
49. M. A. Korhonen, P. Borgesen, D. D. Brown and C.-Y. Li, *J. Appl. Phys.,* **74**(8), 4995-5004 (1993).
50. C.-K. Hu, L. Gignac and R. Rosenberg, *Microelectronics Reliability*, **46**(2-4), 213-231 (2006).
51. C.-C. Lin and Y. Kuo, MRS Online Proceedings Library Archive 1428 (2012).
52. S. W. Goh, A. N. Buckley, R. N. Lamb, R. A. Rosenberg and D. Moran, *Geochimica et Cosmochimica Acta*, **70**(9), 2210-2228 (2006).
53. M. C. Biesinger, L. W. M. Lau, A. R. Gerson and R. St. C. Smart, *Appl. Surface Sci.*, **257**(3), 887-898 (2010).
54. S. Poulston, P. M. Parlett, P. Stone and M. Bowker, *Surface and Interface Analysis*, **24**(12), 811-820 (1996).
55. H. Sun, O. A. Zelekew, X. Chen, Y. Guo, D.-H. Kuo, Q. Lu and J. Lin, *RSC Advances*, **9**(55), 31828-31839 (2019).
56. C. N. Hinshelwood, *Proceedings of the Royal Society of London*, Series A, **102**(716), 318-328 (1922).
57. Y. S. Gong, C. Lee, and C. K. Yang, *J. Appl. Phys.,* **77**(10), 5422-5425 (1995).
58. K. Hinode Y. Hanaoka, K. Takeda and S. Kondo, *Japan J. of Appl. Phys.*, **40**(10B), L1097 (2001).
59. M. Momcilovic, M. Trtica, J. Ciganovic, J. Savovic, J. Stasic and M. Kuzmanovic, *Appl. Surface Science*, **270**, 486-494 (2013).